Research Article

Triethylamine as a tuning agent of the MIL-125 particle morphology and its effect on the photocatalytic activity

Nicolás Artemio Rodríguez[1,2] · Rodrigo Parra[1,3] · María Alejandra Grela[1,2]

Abstract
MIL-125 is prepared using a modified version of a previously reported strategy, in which different ratios of trimethylamine (TEA) are added to the reaction mixture. It is shown that TEA made the synthesis of MIL-125 more feasible, at lower temperatures, and limiting the formation of TiO_2. The solids are then characterized by various means and finally studied in the photodegradation of Rhodamine B (RhB). The shape and size of MIL-125 particles can be tuned by varying the number of TEA equivalents, with the smallest particles yielding the highest rate of RhB decomposition. It is found that the adsorption of the photocatalyst on MIL-125 plays an important role in the photodegradation mechanism of the dye.

Keywords Metal-Organic Frameworks · Photocatalysis · Particle morphology · MIL-125

1 Introduction

Metal-Organic Frameworks (MOFs) are a class of materials with promising properties for many applications [1–3], ranging from gas storage [4] to heterogeneous photocatalysis [5–7]. However, the synthesis and stability of MOFs are still subject to continuous analysis [7–9]. Some of these materials present weak interactions between the metal (or metallic cluster) and the ligands, which makes them prone to hydrolysis, as it is the case of Zn-based MOFs. Nevertheless, these Zn-based materials were the first MOFs to be synthesized at the end of the twentieth century and from their study much insight was gained regarding their strikingly high surface areas [4], the possibility of tuning their properties [10], and some ways to inhibit the hydrolysis of these materials [11].

Other kinds of MOFs were prepared in the years following the first reports. In particular, Ti-based MOFs are interesting because of their higher stability in water or humid conditions, compared to those synthesized using Zn precursors. Dan-Hardi et al. [12] prepared in 2009 a MOF using a Ti precursor for the first time, MIL-125. The synthesis of MIL-125 involved the solvothermal reaction of a mixture of titanium (IV) isopropoxide and terephthalic acid (H_2BDC) in N,N-dimethylformamide (DMF) and methanol. However, it was recognized that the product obtained by this method contained impurities of TiO_2 [12]. In 2013 Hendon et al. [13] obtained MIL-125 by a new strategy, which involved the synthesis of a Ti-oxocluster coordinated by pivalic acid. This solid was then mixed with H_2BDC in DMF and methanol and heated to obtain MIL-125.

✉ Nicolás Artemio Rodríguez, narodriguez@mdp.edu.ar | [1]Departamento de Química, Facultad de Ciencias Exactas y Naturales (FCEyN), Universidad Nacional de Mar del Plata (UNMdP), Dean Funes 3350, B7602AYL, Mar del Plata, Buenos Aires, Argentina. [2]Instituto de Física de Mar del Plata (IFIMAR), CONICET - Universidad Nacional de Mar del Plata, Dean Funes 3350, B7602AYL, Mar del Plata, Buenos Aires, Argentina. [3]Instituto de Investigaciones en Ciencia y Tecnología de Materiales (INTEMA), CONICET - Universidad Nacional de Mar del Plata, Av. Colón 10850, B7606BWV, Mar del Plata, Buenos Aires, Argentina.

The Ti-oxocluster is less reactive than titanium (IV) isopropoxide, which makes it easier to handle. However, this precursor is barely employed in later reports. Titanium isopropoxide [14–23] and titanium t-butoxide [24–31] are currently the preferred precursors in the synthesis of MIL-125 materials or derivatives. In the experience of this group, MIL-125 could be obtained from the Ti-oxocluster only by using PARR reactors, with some syntheses failing to lead the desired material. Other custom-made Teflon-lined reactors were not suitable for the task. For that reason, it is more appealing to turn to other usual titanium precursors which, on the other hand, are more prone to lead to TiO_2 as impurity.

Nevertheless, there are ways to overcome the problems associated with the low reactivity of the reactants in these kinds of syntheses, by adjusting the pH of the mixture. Tranchemontagne et al. [32] obtained several Zn-based MOFs, usually synthesized by heating the reactants to around 120 °C, at room temperature by adding triethylamine to the reaction mixture. However, the ratio of H_2BDC:TEA needs to be regulated, to avoid the hydrolysis of the metallic precursor (Compare the work of Huang et al. [33] with that of Feng et al. [34]). In this context, the present work deals with the synthesis of MIL-125 samples obtained by employing different TEA:H_2BDC ratios in the reaction mixture.

MIL-125 has been employed in a range of photocatalytic applications, mainly in advanced heterostructured materials [16, 35, 36]. Despite its high bandgap, dyes from waste water can be decomposed under visible light with this kind of materials, thanks to the reactions induced from the injection of photogenerated electrons in the dye to the semiconductor, as shown in many works employing TiO_2 [37]. In particular, the photodegradation of Rhodamine B (RhB) is currently an important model to test the activity of new photocatalyst, as proven by the continuous work on the field [38–40], driven by the need of better means for the treatment of waste waters. This studies include the analysis of the morphology of a photocatalyst in its photocatalytic activity [41]. In that sense, it will be shown in this work that the use of different TEA:H_2BDC ratios leads to MIL-125 samples of different particle sizes and shapes, which are analysed by various means. Then, the suitability of each sample for the photocatalytic degradation of RhB is tested and the influence of the morphology on these systems is discussed. It is expected that this work provides an insight in new ways to synthesize MIL-125 by employing the Ti-oxocluster precursor, especially in the preparation of advanced heterostructures whose particles' shape and size play a critical role in its design.

2 Materials and methods

2.1 Chemicals

Titanium (IV) isopropoxide (Sigma-Aldrich), terephthalic acid (Sigma), N,N-dimethylformamide (Sintorgan), methanol (Sintorgan), pivalic acid (Sigma-Aldrich), acetonitrile (Sintorgan), triethylamine (TEA, Sintorgan), and Rhodamine B (RhB, Sigma-Aldrich) were employed as received.

2.2 Synthesis of MIL-125 samples

As stated previously, MIL-125 was obtained from the modified version of the procedure reported by Hendon et al. [13]. The first step involves the isolation of the Ti-oxocluster. This was achieved by dissolving 5 mL of titanium (IV) isopropoxide and 17.5 g of pivalic acid in 60 mL of acetonitrile. The solution was heated at 120 °C during 3 days in a Teflon-lined stainless steel reactor. The solid product was then washed with small volumes of acetonitrile and dried in atmospheric conditions.

MIL-125 was obtained by dissolving 1.13 g of the Ti-oxocluster and 1.4 g of H_2BDC in 68 mL of DMF and 22 mL of methanol. Different amounts of TEA were added to the solution to obtain different samples: 0, 1, 2, 3 and 4 equivalents (0 mL, 1.2 mL, 2.4 mL, 3.5 mL and 4.7 mL of TEA, respectively). Reaction mixtures were heated at 120 °C during 3 days, and a second mixture with 2 equivalents of TEA in the reaction mixture was heated during 7 days. Table 1 presents the name of each sample according to the amount of TEA used and the time of reaction. The solids were then washed with DMF first and then methanol to be finally dried at room temperature.

2.3 Characterization

X-ray powder diffraction (XRD) patterns were obtained from a PANalytical X'Pert diffractometer under Kα copper radiation. Themogravimetric analysis were carried out on a Shimadzu TG-50 instrument under a synthetic air flow.

Table 1 Names of the prepared samples

Equivalents of TEA	Reaction time (days)	Sample name	Colour code
0	3	MIL-125_TEA0	Brown
1	3	MIL-125_TEA1	Green
2	3	MIL-125_TEA2	Red
2	7	MIL-125_TEA2_7d	Black
3	3	MIL-125_TEA3	Blue
4	3	MIL-125_TEA4	Orange

FTIR spectra were acquired on a PerkinElmer Spectrum BX II FTIR spectrometer equipped with an attenuated total reflection (ATR) unit and Raman spectra were obtained by means of a Renishaw inVia spectrometer equipped with a near-IR (785 nm) excitation diode laser.

Optical absorptance spectra of powders were measured on a Shimadzu UV-2450 spectrophotometer equipped with an integrating sphere. As shown in a previous report [7] the ratio of absorbed light, or absorptance $\alpha(\lambda)$ is calculated from the reflectance, $R(\lambda)$, and the transmittance, $T(\lambda)$, of the sample as follows:

$$\alpha(\lambda) = 1 - R(\lambda) - T(\lambda) \tag{1}$$

Scanning electron microscopy (SEM) images were obtained on a LEO 1550-Gemini. Particle size was measured using a Zetasizer Nano S90 (Malvern). The absorption spectra of RhB solutions for were recorded on an Agilent 8453—G1103A UV/vis spectrophotometer.

2.4 Photodegradation of Rhodamine B

Fifteen milligrams of the photocatalyst were dispersed in 15 mL of a 100 mg L^{-1} aqueous solution of RhB. The resulting dispersion was stirred for 2 h in the dark to allow the adsorption of the dye. Then, the dispersion was irradiated with a blue LED lamp emitting at 470 nm (50 W, Epistar). Aliquots of 125 µL of the irradiated dispersion were taken at different irradiation times, diluted with 1050 µL of water and centrifuged (12,000 rpm, 5 min). 1000 µL of the supernatant were taken and diluted with another 1000 µL of water. The solutions were then analysed by UV–Vis light spectrometry to follow the decay of RhB concentration as a function of irradiation time, by measuring its absorption at 550 nm.

Adsorption isotherms were obtained to analyse whether the adsorption of the dye plays a role in its photodegradation rate. This was achieved by dispersing 5 mg of the MIL-125 samples in different volumes of RhB 1000 mg L^{-1} (between 100 and 750 µL). The solutions were diluted to a total volume of 5 mL and agitated under dark during 2 h. Small aliquots were taken, centrifuged (12,000 rpm, 5 min), diluted in a 1:20 ratio and analysed by UV/Vis spectroscopy to determine the amount of free RhB.

3 Results and discussion

3.1 Characterization of the samples

The solids were analysed by X-Ray diffraction to determine the crystalline phases present in each material, as seen in Fig. 1. It is observed that the samples obtained
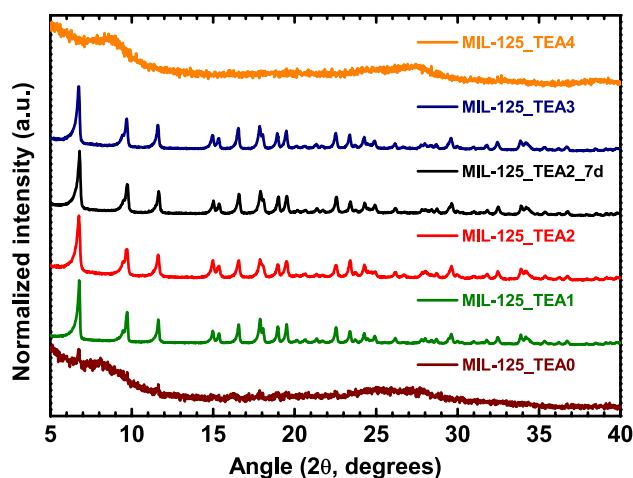

Fig. 1 XRD patterns of the synthesized solids. Colour codes in Table 1

by using between 1 and 3 equivalents of TEA show the characteristic peaks of MIL-125. On the other hand, the samples MIL-125_TEA0 and MIL-125_TEA4 only present a few broad peaks. A closer inspection to the XRD pattern of MIL-125_TEA0 shows that it actually presents the two most intense peaks corresponding to MIL-125. Further analyses were carried out on the samples to explain the differences.

It can be concluded, from the XRD patterns, that the use of TEA allows the synthesis of MIL-125 at a lower temperature than the initially reported (120 °C against 150 °C). In fact, it was found that MIL-125 can also obtained by heating the reaction mixture at only 80 °C during 4 days (data not shown).

To understand the effect of the concentration of TEA in the morphology of the solids, the crystallite size of each MIL-125 sample was determined by analysing the peaks at $2\theta = 16.57°$, $18.97°$ and $19.51°$. The width at half of the peak was found by adjusting Gaussian functions to each signal. The uncertainty of the crystallite size (Δt) was estimated from the standard deviation in the fitting of the Gaussian function (Δt_G) and the standard deviation of the mean value obtained from the three peaks (Δt_P) according to the equation:

$$\Delta t^2 = \Delta t_G{}^2 + \Delta t_P{}^2 \tag{2}$$

The effect of TEA on crystallite size is not monotonic (Table 2) and the uncertainty of the measurements has the same order of magnitude as the differences between some of the estimated crystallite sizes. However, ANOVA analysis shows that there are statistical differences between some of the mean crystallite sizes (p = 0.041). This point will be revisited when analysing the effect on RhB degradation. Besides, it appears that the addition of 3 equivalents of

Table 2 Crystallite size of MIL-125 samples

Sample	Crystallite size (nm)
MIL-125_TEA1	58 ± 5
MIL-125_TEA2	44 ± 4
MIL-125_TEA2_7d	49 ± 5
MIL-125_TEA3	50 ± 5
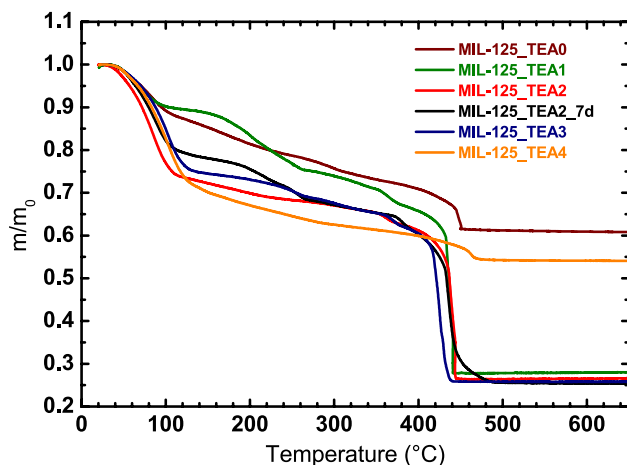
Fig. 2 Thermograms of the synthesized solids. Colour codes in Table 1

**Table 3** Content of Ti (as TiO_2) of each MIL-125 sample

Sample	XRD pattern	TiO_2 content (%)
MIL-125_TEA0	Amorphous/low cryst.	86
MIL-125_TEA1	MIL-125	42
MIL-125_TEA2	MIL-125	43
MIL-125_TEA2_7d	MIL-125	42
MIL-125_TEA3	MIL-125	43
MIL-125_TEA4	Amorphous/low cryst.	90

TEA to the reaction mixture has the same effect as the addition of 2 equivalents, provided that a reaction time of 7 days is employed in the latter case. It will be shown that this trend will be also seen in the analysis of particle sizes and shapes.

Thermogravimetric analyses (Fig. 2) were performed in order to analyse the compositions of the MIL-125 samples. The weight loss below 200 °C is ascribed to the loss of solvent molecules adsorbed at the materials' surface. The ratio of Ti as TiO_2 was determined from the weight at 500 °C divided to that at 400 °C, before the decomposition of MIL-125. Table 3 summarizes the content of titanium as
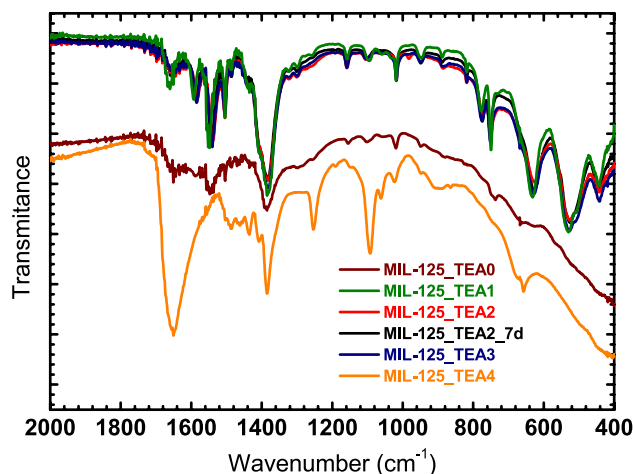
Fig. 3 FTIR of the obtained samples. The spectra of MIL-125_TEA0 and MIL-125_TEA4 were displaced for better visualization. Colour codes in Table 1

TiO_2 estimated for each sample. As a reference, the combustion reaction of MIL-125 is:

$$Ti_8O_8(OH)_4(C_8H_4O_4)_6 + 45\,O_2 \rightarrow 8\,TiO_2 + 48\,CO_2 + 14\,H_2O \tag{3}$$
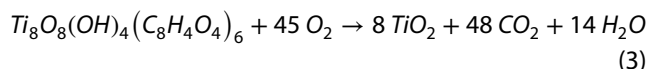
Eight units of TiO_2 represent the 41% of the weight of MIL-125. Samples presenting the XRD pattern of MIL-125 are composed of 42% and 43% of TiO_2. However, the other two samples showed more than 85% of TiO_2 in their compositions.

FTIR spectra of these two samples also differ substantially from the rest (Fig. 3). The solids with XRD patterns matching that of MIL-125 show very similar FTIR spectra between them, which are in accordance to previous reports [12]. MIL-125_TEA0 shows the typical bands of the ligand at 1545 and 1385 cm^{-1} (C=O stretching), which allow to infer that a small amount of MIL-125 has been formed. Bands near 950 cm^{-1} and 635 cm^{-1} are usually adscribed to C-O and Ti-O stretching [42].

On the other hand, MIL-125_TEA4 shows very different FTIR signals. These bands suggest the presence of other species in the sample. This could be accounted by the fact that the excess of TEA can induce the decomposition of DMF at high temperatures, and the products of that reaction may remain trapped within the MOF. The fact MIL-125-TEA4 presents a yellowish colour, is also indicative of the hydrolysis of the solvent. This trend was previously reported in the synthesis of MOF-5 [8].

In that sense, UV-Vis spectra of the solids (Fig. 4) show that the crystalline samples have absorption edges near 350 nm, whereas MIL-125_TEA4 absorbs in visible region of the spectrum. From this information, it can be concluded that only samples obtained using 1–3 equivalents
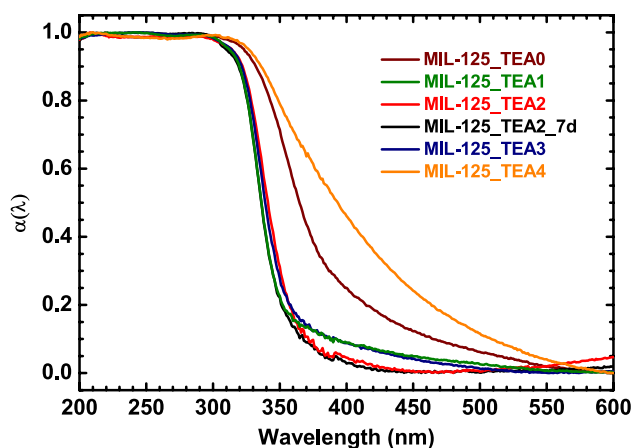
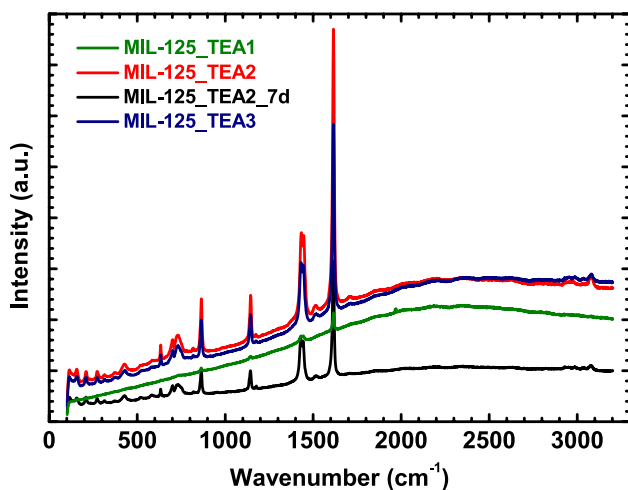**Fig. 4** DRUV spectra of the MIL-125 samples. Colour codes in Table 1

Fig. 5 Raman spectra of the MIL-125 samples. Colour codes in Table 1

of TEA are made of MIL-125. For that reason, the analysis that follows focuses on those specific solids.

All MIL-125 samples showed very similar Raman spectra (Fig. 5), except for that of MIL-125_TEA1, which showed a considerable less intense spectrum than the rest. MIL-125_TEA2 presents the most intense bands. The most intense band at 1617 cm^{-1} is located in the region corresponding to H-O-H of H_2O (adsorbed on the solid) [42]. It is known [43, 44] that the intensity of Raman signals decreases with the increase of particle size, and this trend shows that there is a correlation between particle size and crystallite size.

To further characterize the morphology of the particles of the different samples, SEM analyses were carried out (Fig. 6, complementary pictures displayed in Fig. S1) and the results are summarized in Table 4. From these

results, three different morphologies can be distinguished. First, MIL-125_TEA1 is formed of quasi cubic particles of approximately 450 nm width. On the other hand, MIL-125_TEA2_7d and MIL-125_TEA3 samples are very similar between them: they are constituted by particles with a width of 230 nm and between a third or a half of the depth. Particles of MIL-125_TEA2 seem to have the similar features of the last two samples, but with a smaller average size. However, the shape is not completely defined and the diameter of the particles is around 130 nm. Table 4 shows the estimated widths of the samples from pictures in Fig. 6.

The determination of the particle size was complemented by measurements of dynamic light scattering (DLS) whose results can be seen in Fig. 7 and are also summarized in Table 4. In general, the particle sizes determined via DLS analysis are higher than those obtained from SEM images, except for MIL-125_TEA1. This could be explained by the fact that MIL-125_TEA1 particles have the smallest aspect ratio and, therefore, resemble more closely a sphere. In the other samples, the observed size is in fact the radius of gyration, which deviates from the width and depth when the particles are less spherical [45]. However, both methods show the same trend. It is noteworthy that the DLS analysis of MIL-125_TEA2_7d shows the presence of some particles 90 nm wide. In fact, some small particles can be observed in the respective SEM image, but they do not seem to account for a considerable ratio of the sample.

Table 4 shows that particle sizes are correlated with crystallite sizes. Thus, the sample prepared by using only 1 equivalent of TEA shows the biggest particles and the biggest crystallites. And, correspondingly, both MIL-125_TEA2_7d and MIL-125_TEA3 present similar particle sizes and morphologies, while MIL-125_TEA2 presents both the smallest crystallites and particle size.

As a summary, the number of equivalents of TEA have a remarkable influence on the shape and size of MIL-125 particles. It has been seen that increasing the number of TEA equivalents from 1 to 2 increases dramatically the nucleation speed, reducing the size of the particles. However, further increase from 2 to 3 equivalents seem to favour crystal growth, as its effect is the same of increasing the time of reaction of a batch with 2 TEA equivalents to 7 days. The reaction conditions explored are not exhaustive, which means that further work could be employed to identify other conditions for the preparation of MIL-125 particles depending on the application or desired properties. It is noteworthy that the controlled use of TEA facilitated the synthesis of a crystalline MIL-125 in custom made reactors, previously not suitable for the task. Aside, this approach is an alternative to other strategies recently employed in the synthesis of MIL-125 or derivatives. Depending on the conditions of reaction, previous works have obtained samples with some of the

Fig. 6 SEM images of (**a**) MIL-125_TEA1, (**b**) MIL-125_TEA2, (**c**) MIL-125_TEA2_7d and (**d**) MIL-125_TEA3
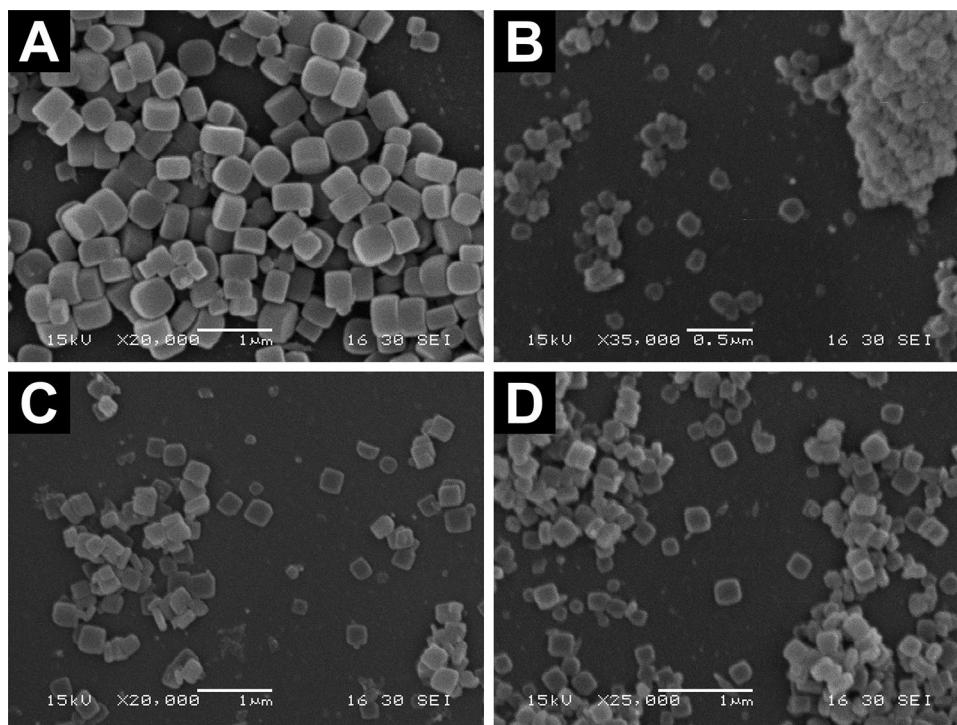

Table 4 Summary of the particle sizes of the MIL-125 samples, obtained from SEM images and DLS analysis

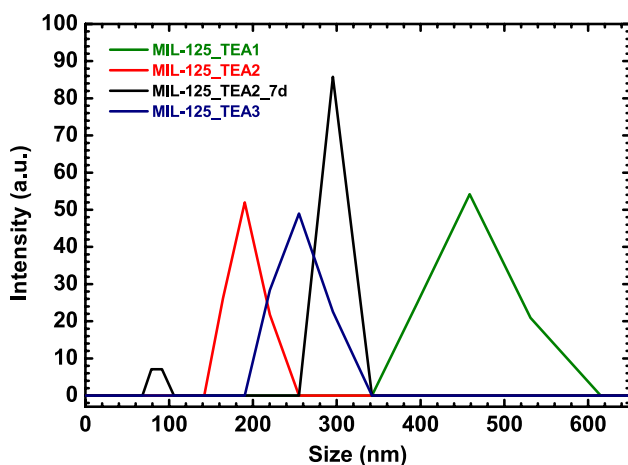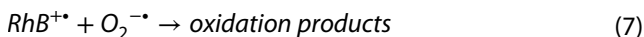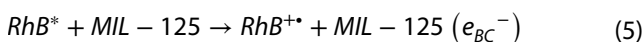| Sample	Width (SEM, nm) (N° of measurements)	Depth (SEM, nm) (N° of measurements)	Aspect ratio	Size (DLS, nm)
MIL-125_TEA1	450 ± 40 **(16)**	285 ± 32 **(19)**	1.6	460 ± 110
MIL-125_TEA2	130 ± 20 **(16)**	57 ± 2 **(3)**	2.3	190 ± 50
MIL-125_TEA2_7d	230 ± 20 **(23)**	79 ± 13 **(6)**	3.0	300 ± 40
MIL-125_TEA3	230 ± 20 **(19)**	107 ± 13 **(10)**	2.2	250 ± 80

Fig. 7 Particle size profiles of relevant MIL-125 samples. Colour codes in Table 1

morphologies here reported, like MIL-125_TEA1 [16, 18, 20] or MIL-125_TEA3 [14, 17] (as mentioned in the Sect. 1, without using the Ti-oxocluster as a precursor). It should be pointed out that Hu et al. [21] made an extensive analysis of how to control particle shape and size by adding mono-functionalized ligands in the reaction mixture. This work is a complement of that work in the sense that they employed aminoterephthalic acid as the organic precursor, instead of terephthalic acid. That change not only influence the optical properties of the solid (usually named as MIL-125-NH$_2$) but we have detected that the presence of the amino functionality allows the synthesis of MIL-125-NH$_2$ from the Ti-oxocluster without the need of TEA [6]. For that reason, this approach to the size and shape control not only complements previous reports, but it is a viable strategy to the synthesis of MIL-125 in conditions which minimize the presence of TiO$_2$ because of the use of the Ti-oxocluster.

3.2 Photocatalytic activity

After the synthesis and characterization of MIL-125, its performance in the photocatalytic decomposition of RhB was analysed. Figure 8 shows the degradation curves of RhB, typical C/C_0 runs can be seen in Fig. S2. It was determined that the dye does not decompose in the absence of light or the photocatalyst. The solids were analysed *via* XRD and no significant changes were observed (Fig. S3). Because MIL-125 does not absorb blue light, the central step in the mechanism of RhB photodegradation is the injection of electrons from the excited Rhodamine B (RhB*) to the catalyst, as represented by steps (4) and (5). This means that not only holes (h+) are not expected to play a significant role in the RhB degradation, but neither ˙OH radicals, as this group is formed by the reaction of holes with organic molecules [46]. The electrons in MIL-125 are then transferred to the oxygen in the solution (6) to form radicals which further the oxidation of the dye (7) [37].

$$RhB + h\nu \rightarrow RhB^* \tag{4}$$

$$RhB^* + MIL - 125 \rightarrow RhB^{+\bullet} + MIL - 125\left(e_{BC}^-\right) \tag{5}$$

$$MIL - 125\left(e_{BC}^-\right) + O_2 \rightarrow MIL - 125 + O_2^{-\bullet} \tag{6}$$

$$RhB^{+\bullet} + O_2^{-\bullet} \rightarrow oxidation\ products \tag{7}$$

Under this mechanism, the effect of the photocatalyst is given, on the one side, by the competition between the injection of electrons from RhB* to MIL-125 and the relaxation of the excited RhB molecules:
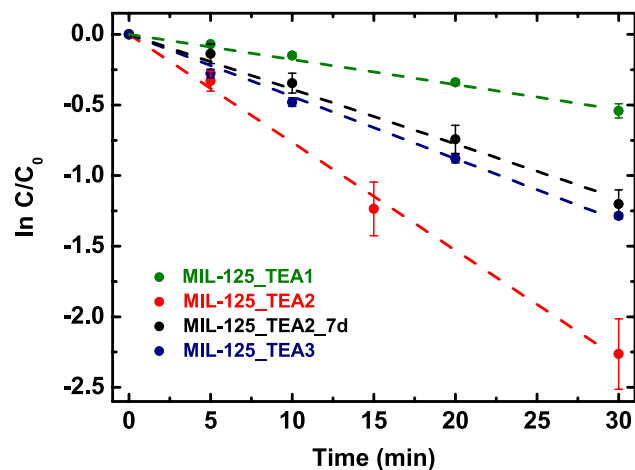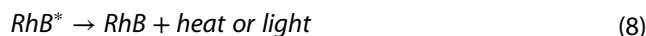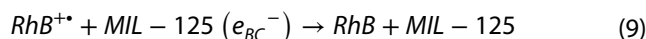
$$RhB^* \rightarrow RhB + heat\ or\ light \tag{8}$$

Aside, there is the competition between the transfer of electrons from MIL-125 conduction band to dissolved oxygen and the electron backtransfer to oxidized RhB:

$$RhB^{+\bullet} + MIL - 125\left(e_{BC}^-\right) \rightarrow RhB + MIL - 125 \tag{9}$$

As the rate of decomposition is exponential, the logarithm of the dye concentration is plotted to find the reaction rate. It is found that there is an inverse correlation between the crystallite size and the particle size with the degradation rate of RhB (Fig. 9a and b, respectively). This can be due to two different reasons. One of them is the higher surface area of the samples with the smallest particles. In fact, the adsorption isotherms (Fig. 10) show that MIL-125_TEA2 (which has the highest rate of dye
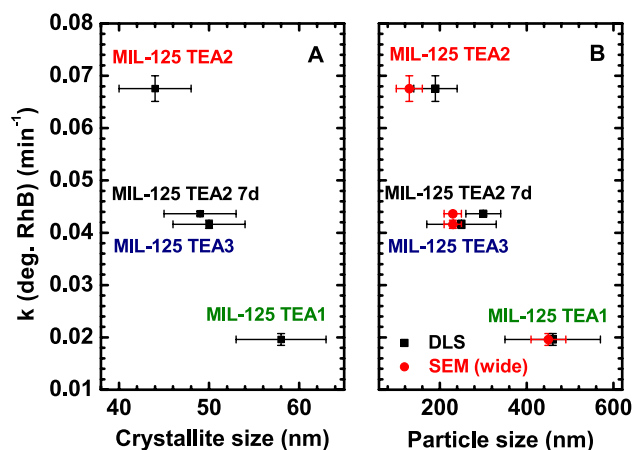
Fig. 9 Correlation between rate constants and (**a**) crystallite size, (**b**) particle size of MIL-125 samples. Colour codes in Table 1

Fig. 8 Degradation curves of RhB in presence of different photocatalysts. Colour codes in Table 1
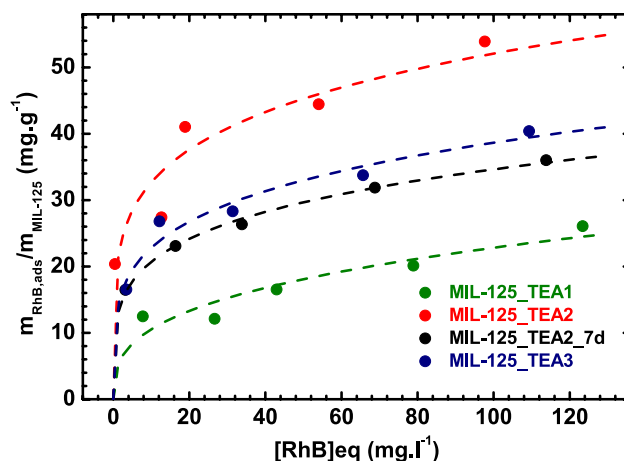
Fig. 10 Adsorption isotherms of RhB by the different MIL-125 samples. Colour codes in Table 1

degradation) is the material which adsorbs the highest amount of RhB. Accordingly, MIL-125_TEA2_7d and MIL-125_TEA3 adsorbs similar amounts of Rhodamine B and degrade it at a similar rate, while MIL-125_TEA1 is the material which adsorbs the lowest amount of dye and has the smallest photodegradation rate of RhB. A higher adsorption of RhB favors the step (5), increasing the rate of RhB decomposition.

The crystallite size may also influence the degradation rate of RhB. The effect of the different crystallite sizes may be the trapping of the injected electrons to the conduction band of MIL-125, which inhibits step (9). However, the correlation seems to be less pronounced. In fact, the mean crystallite size of MIL-125_TEA2 is not statistically different from MIL-125_TEA2_7d (p = 0.12), however, the adjusted rate constants are considerably different. On the other hand, the difference between the mean particle size is significant for any two of the three groups of samples discussed, correspondingly to the difference between the rate constants.

4 Conclusions

It has been observed that TEA makes the synthesis of MIL-125 (from a Ti-oxocluster) possible in milder conditions, and that the $H_2BDC:TEA$ ratio influences the morphology of the resulting particles. Both reaction time and temperature play an important role in the final shape of the particles, and can be reliably tuned in order to obtain the desired product. This difference in morphology greatly influences the rate of photo-oxidation of Rhodamine B by MIL-125 under blue light. The main cause for these changes seem to be the absorption of the target molecule, favoured by smaller particles.

As the Ti-oxocluster is less reactive than other widespread precursors and it is not usually employed, there is room for improvement in the optimization of reactions conditions, in which TEA can be one of the variables to tune, according to the desired application. In particular, it is noteworthy that the optimal particle size of MIL-125 samples for RhB degradation is obtained at an intermediate ratio of TEA (2 equivalents).

Compliance with ethical standards

Conflict of interest The authors report that there are no conflicts of interest to declare.

References

1. Huxford RC, Della Rocca J, Lin W (2010) Metal–organic frameworks as potential drug carriers. Curr Opin Chem Biol 14:262–268. https://doi.org/10.1016/j.cbpa.2009.12.012
2. Czaja AU, Trukhan N, Müller U (2009) Industrial applications of metal–organic frameworks. Chem Soc Rev 38:1284. https://doi.org/10.1039/b804680h
3. Liu J, Chen L, Cui H et al (2014) Applications of metal–organic frameworks in heterogeneous supramolecular catalysis. Chem Soc Rev 43:6011–6061. https://doi.org/10.1039/C4CS00094C
4. Furukawa H, Cordova KE, O'Keeffe M, Yaghi OM (2013) The chemistry and applications of metal-organic frameworks. Science 341:1230444. https://doi.org/10.1126/science.1230444
5. Li Y, Xu H, Ouyang S, Ye J (2016) Metal–organic frameworks for photocatalysis. Phys Chem Chem Phys 18:7563–7572. https://doi.org/10.1039/C5CP05885F
6. Rodríguez NA, Savateev A, Grela MA, Dontsova D (2017) Facile synthesis of potassium poly(heptazine imide) (PHIK)/Ti-based metal–organic framework (MIL-125-NH$_2$) composites for photocatalytic applications. ACS Appl Mater Interfaces 9:22941–22949. https://doi.org/10.1021/acsami.7b04745
7. Rodríguez NA, Parra R, Grela MA (2015) Structural characterization, optical properties and photocatalytic activity of MOF-5 and its hydrolysis products: implications on their excitation mechanism. RSC Adv 5:73112–73118. https://doi.org/10.1039/C5RA11182J
8. Kaye SS, Dailly A, Yaghi OM, Long JR (2007) Impact of preparation and handling on the hydrogen storage properties of $Zn_4O(1,4$-benzenedicarboxylate$)_3$ (MOF-5). J Am Chem Soc 129:14176–14177. https://doi.org/10.1021/ja076877g
9. McKinstry C, Cussen EJ, Fletcher AJ et al (2013) Effect of synthesis conditions on formation pathways of metal organic framework (MOF-5) crystals. Cryst Growth Des 13:5481–5486. https://doi.org/10.1021/cg4014619
10. Eddaoudi M, Kim J, Rosi N et al (2002) Systematic design of pore size and functionality in isoreticular MOFs and their application in methane storage. Science 295:469–472. https://doi.org/10.1126/science.1067208
11. Wu C-M, Rathi M, Ahrenkiel SP et al (2013) Facile synthesis of MOF-5 confined in SBA-15 hybrid material with enhanced hydrostability. Chem Commun 49:1223. https://doi.org/10.1039/c2cc38366g
12. Dan-Hardi M, Serre C, Frot T et al (2009) A new photoactive crystalline highly porous titanium(IV) dicarboxylate. J Am Chem Soc 131:10857–10859. https://doi.org/10.1021/ja903726m
13. Hendon CH, Tiana D, Fontecave M et al (2013) Engineering the optical response of the titanium-MIL-125 metal-organic framework through ligand functionalization. J Am Chem Soc 135:10942–10945. https://doi.org/10.1021/ja405350u
14. Oveisi M, Asli MA, Mahmoodi NM (2018) MIL-Ti metal-organic frameworks (MOFs) nanomaterials as superior adsorbents: synthesis and ultrasound-aided dye adsorption from multicomponent wastewater systems. J Hazard Mater 347:123–140. https://doi.org/10.1016/j.jhazmat.2017.12.057
15. Wang F, He X, Sun L et al (2018) Engineering an N-doped TiO_2@N-doped C butterfly-like nanostructure with long-lived photo-generated carriers for efficient photocatalytic selective amine oxidation. J Mater Chem A 6:2091–2099. https://doi.org/10.1039/C7TA09166D
16. Zhaohui H, Hui C, Lei Z et al (2018) Biogenic hierarchical MIL-125/TiO$_2$@SiO$_2$ derived from rice husk and enhanced photocatalytic properties for dye degradation. Photochem Photobiol. https://doi.org/10.1111/php.12873

17. Fan Y-H, Zhang S-W, Qin S-B et al (2018) An enhanced adsorption of organic dyes onto NH_2 functionalization titanium-based metal-organic frameworks and the mechanism investigation. Microporous Mesoporous Mater 263:120–127. https://doi.org/10.1016/j.micromeso.2017.12.016

18. Ji P, Song Y, Drake T et al (2018) Titanium(III)-oxo clusters in a metal–organic framework support single-site Co(II)-hydride catalysts for arene hydrogenation. J Am Chem Soc 140:433–440. https://doi.org/10.1021/jacs.7b11241

19. Logan MW, Adamson JD, Le D, Uribe-Romo FJ (2017) Structural stability of N-alkyl-functionalized titanium metal–organic frameworks in aqueous and humid environments. ACS Appl Mater Interfaces 9:44529–44533. https://doi.org/10.1021/acsami.7b15045

20. Liao Y-T, Huang Y-Y, Chen HM et al (2017) Mesoporous TiO_2 embedded with a uniform distribution of CuO exhibit enhanced charge separation and photocatalytic efficiency. ACS Appl Mater Interfaces 9:42425–42429. https://doi.org/10.1021/acsami.7b13912

21. Hu S, Liu M, Guo X et al (2017) Effects of monocarboxylic acid additives on synthesizing metal–organic framework NH_2-MIL-125 with controllable size and morphology. Cryst Growth Des 17:6586–6595. https://doi.org/10.1021/acs.cgd.7b01250

22. Vilela S, Salcedo-Abraira P, Colinet I et al (2017) Nanometric MIL-125-NH_2 metal–organic framework as a potential nerve agent antidote carrier. Nanomaterials 7:321. https://doi.org/10.3390/nano7100321

23. Abdelhameed RM, Tobaldi DM, Karmaoui M (2018) Engineering highly effective and stable nanocomposite photocatalyst based on NH_2-MIL-125 encirclement with Ag_3PO_4 nanoparticles. J Photochem Photobiol A Chem 351:50–58. https://doi.org/10.1016/j.jphotochem.2017.10.011

24. Duan D, Yang H, Ding Y et al (2018) Three-dimensional molecularly imprinted electrochemical sensor based on Au NPs@Ti-based metal-organic frameworks for ultra-trace detection of bovine serum albumin. Electrochim Acta 261:160–166. https://doi.org/10.1016/j.electacta.2017.12.146

25. Ingole PG, Sohail M, Abou-Elanwar AM et al (2018) Water vapor separation from flue gas using MOF incorporated thin film nanocomposite hollow fiber membranes. Chem Eng J 334:2450–2458. https://doi.org/10.1016/j.cej.2017.11.123

26. Liu H, Zhang J, Ao D (2018) Construction of heterostructured $ZnIn_2S_4$@NH_2-MIL-125(Ti) nanocomposites for visible-light-driven H_2 production. Appl Catal Environ 221:433–442. https://doi.org/10.1016/j.apcatb.2017.09.043

27. Zhou G, Wu M-F, Xing Q-J et al (2018) Synthesis and characterizations of metal-free Semiconductor/MOFs with good stability and high photocatalytic activity for H_2 evolution: a novel Z-Scheme heterostructured photocatalyst formed by covalent bonds. Appl Catal Environ 220:607–614. https://doi.org/10.1016/j.apcatb.2017.08.086

28. Zhu S-R, Wu M-K, Zhao W-N et al (2017) Fabrication of heterostructured $BiOBr$/$Bi_{24}O_{31}Br_{10}$/TiO_2 photocatalyst by pyrolysis of MOF composite for dye degradation. J Solid State Chem 255:17–26. https://doi.org/10.1016/j.jssc.2017.07.038

29. Shi X, Liu S, Tang B et al (2017) SnO_2/TiO_2 nanocomposites embedded in porous carbon as a superior anode material for lithium-ion batteries. Chem Eng J 330:453–461. https://doi.org/10.1016/j.cej.2017.07.164

30. Ye F, Li H, Yu H et al (2017) Hydrothermal fabrication of few-layer MoS_2 nanosheets within nanopores on TiO_2 derived from MIL-125(Ti) for efficient photocatalytic H_2 evolution. Appl Surf Sci 426:177–184. https://doi.org/10.1016/j.apsusc.2017.07.087

31. Hong Z, Kang M, Chen X et al (2017) Synthesis of mesoporous Co^{2+}-doped TiO_2 nanodisks derived from metal organic frameworks with improved sodium storage performance. ACS Appl Mater Interfaces 9:32071–32079. https://doi.org/10.1021/acsami.7b06290

32. Tranchemontagne DJ, Hunt JR, Yaghi OM (2008) Room temperature synthesis of metal-organic frameworks: MOF-5, MOF-74, MOF-177, MOF-199, and IRMOF-0. Tetrahedron 64:8553–8557. https://doi.org/10.1016/j.tet.2008.06.036

33. Huang L (2003) Synthesis, morphology control, and properties of porous metal–organic coordination polymers. Microporous Mesoporous Mater 58:105–114. https://doi.org/10.1016/S1387-1811(02)00609-1

34. Feng PL, Perry JJ IV, Nikodemski S et al (2010) Assessing the purity of metal–organic frameworks using photoluminescence: MOF-5, ZnO quantum dots, and framework decomposition. J Am Chem Soc 132:15487–15489. https://doi.org/10.1021/ja1065625

35. An Y, Xu B, Liu Y et al (2017) Photocatalytic overall water splitting over MIL-125(Ti) upon CoPi and Pt co-catalyst deposition. ChemistryOpen 6:701–705. https://doi.org/10.1002/open.201700100

36. Yuan X, Wang H, Wu Y et al (2016) One-pot self-assembly and photoreduction synthesis of silver nanoparticle-decorated reduced graphene oxide/MIL-125(Ti) photocatalyst with improved visible light photocatalytic activity. Appl Organomet Chem 30:289–296. https://doi.org/10.1002/aoc.3430

37. Konstantinou IK, Albanis TA (2004) TiO_2-assisted photocatalytic degradation of azo dyes in aqueous solution: kinetic and mechanistic investigations. Appl Catal Environ 49:1–14. https://doi.org/10.1016/j.apcatb.2003.11.010

38. Wang W, Cheng B, Yu J et al (2012) Visible-light photocatalytic activity and deactivation mechanism of Ag_3PO_4 spherical particles. Chem Asian J 7:1902–1908. https://doi.org/10.1002/asia.201200197

39. Rodríguez NA, Savateev A, Grela MA, Dontsova D (2017) In-situ prepared potassium poly(heptazine imide) (PHIK)/Ti-based Metal-Organic Framework (MIL-125-NH_2) composites for photocatalytic applications (enviado). ACS Appl Mater Interfaces 9(27):22941–22949

40. Dong P, Hou G, Xi X et al (2017) WO_3-based photocatalysts: morphology control, activity enhancement and multifunctional applications. Environ Sci Nano 4:539–557. https://doi.org/10.1039/C6EN00478D

41. Xu D, Jiang T, Wang D et al (2014) pH-dependent assembly of tungsten oxide three-dimensional architectures and their application in photocatalysis. ACS Appl Mater Interfaces 6:9321–9327. https://doi.org/10.1021/am501651m

42. Liu Z, Wu Y, Chen J et al (2018) Effective elimination of As(III) via simultaneous photocatalytic oxidation and adsorption by a bifunctional cake-like TiO_2 derived from MIL-125(Ti). Cat Sci Technol 8:1936–1944. https://doi.org/10.1039/C8CY00125A

43. Pellow-Jarman MV, Hendra PJ, Lehnert RJ (1996) The dependence of Raman signal intensity on particle size for crystal powders. Vib Spectrosc 12:257–261. https://doi.org/10.1016/0924-2031(96)00023-9

44. Michalska M, Krajewski M, Ziolkowska D et al (2014) Influence of milling time in solid-state synthesis on structure, morphology and electrochemical properties of $Li_4Ti_5O_{12}$ of spinel structure. Powder Technol 266:372–377. https://doi.org/10.1016/j.powtec.2014.06.056

45. Berne BJ, Pecora R (2000) Molecules of arbitrary shape. In: Dynamic light scattering: with applications to chemistry, biology, and physics. Wiley, New York, pp 169–171

46. Cheng L, Xiang Q, Liao Y, Zhang H (2018) CdS-Based photocatalysts. Energ Environ Sci 11:1362–1391. https://doi.org/10.1039/C7EE03640J